Constraints on subducting plate strength within the Kermadec trench

Magali I. Billen
Department of Geology, University of California, Davis, California, USA

Michael Gurnis
Seismological Laboratory, California Institute of Technology, Pasadena, California, USA

Received 8 July 2004; revised 23 January 2005; accepted 11 February 2005; published 24 May 2005.

[1] Four specially designed surveys parallel to the Kermadec trench allow localized estimates of plate strength within the subducting Pacific plate to be made. The transfer function between topography and gravity is estimated for five trench-parallel ship tracks at distances of 25–110 km from the trench axis. We find a clear reduction in the magnitude and peak wavelength of the transfer function from the outer rise to the trench axis. The change in the transfer function indicates a decrease in plate strength and is consistent with a reduction in flexural rigidity by 3–5 orders of magnitude or a decrease in effective elastic thickness by more than 15 km. Such a large-magnitude decrease in the effective elastic strength suggests that the plate has little or no elastic strength within the trench and that viscous stresses play an important role in transferring slab-pull forces to the subducting plate and regulating plate speeds in subduction zones.

Citation: Billen, M. I., and M. Gurnis (2005), Constraints on subducting plate strength within the Kermadec trench, *J. Geophys. Res.*, *110*, B05407, doi:10.1029/2004JB003308.

1. Introduction

[2] Oceanic plates represent the top thermal boundary layer of mantle convection [*Davies and Richards*, 1992]. However, unlike isoviscous fluid convection the top thermal boundary layer on Earth is divided into rigid tectonic plates separated by narrow zones of weakness, which include divergent, convergent and strike-slip boundaries. The strength of the plate interiors and weakness of the plate margins are controlled by complex rheologies, which can lead to permanent zones of weakness. The cold slowly deforming interior of the plate is stiff and behaves elastically, but it may yield ductilely or flow viscously under large stress, while the shallow crust responds through brittle fracture [*Goetze and Evans*, 1979; *Evans et al.*, 1990; *Kohlstedt et al.*, 1995]. Both permanent zones of weakness, and instantaneous deformation and weakening of the plates play an important role in determining how tectonic plates couple to convective flow in the Earth's mantle [*Gurnis et al.*, 2000].

[3] The negative buoyancy of a sinking slab is both the force pulling the plate into the mantle and the stress acting to deform and weaken the plate as it bends in the subduction zone. Bending of the plate may account for a substantial fraction of the total energy dissipation associated with plate motion [*Conrad and Hager*, 2001]. As the plate weakens less of the slab-pull force is able to couple to the plate at the surface [*Conrad and Lithgow-Bertelloni*, 2002; *Billen et al.*, 2003]. Therefore the width of the deformation zone and magnitude of weakening at converging plate margins have important implications for coupling of the slab-pull force to the subducting plate and for constraining the processes that regulate plate speeds (e.g., dissipation of viscous, frictional and fracture energy).

[4] Deformation of subducting plates in convergent margins has been study extensively using plate bending models that predict the shape of the plate perpendicular to the trench. In particular, the ability of these models to reproduce the outer rise (a topographic rise of ~200 m in height oceanward of the trench) using elastic or elastic-plastic rheology requires plate stresses exceeding 500 MPa [*McAdoo et al.*, 1978; *Chapple and Forsyth*, 1979] and suggests that the plate remains quite strong within the subduction zone. However, it has also been shown that plate-bending models [*DeBremaecker*, 1977; *Melosh*, 1978] and geodynamic models [*Zhong et al.*, 1998; *Gurnis et al.*, 2000] using viscous rheology also reproduce the trench topography, including the outer rise as a dynamically maintained feature at low stress. Contrary to the elastic plate models, the success of these viscous models indicates that the oceanic lithosphere may not retain any elastic strength within the subduction zone. Plate bending models, however, are not sensitive to variations in plate strength along the profile and only provide a measure of average plate properties over the length scale of bending [*Judge and McNutt*, 1991]. Direct measurement of the deformation zone is needed to constrain the variation in plate strength within convergent margins.

[5] Observations of seafloor bathymetry and seismic reflection data at several subduction zones demonstrate that subducting plates suffer significant crustal-scale faulting

0148-0227/05/2004JB003308$09.00

while entering the trench [*Jones et al.*, 1978; *Masson*, 1991; *Kobayashi et al.*, 1998; *Massell*, 2003; *Ranero et al.*, 2003]. Large tensional earthquakes, which cut though the 100 km thick lithosphere, also occur in the subducting plate below the plate boundary and the outer rise [*Kikuchi and Kanamori*, 1995; *Christensen and Ruff*, 1988]. Contrary to conventional models of elastic plate bending, these earthquakes indicate that the subducting plate undergoes permanent, lithosphere-scale deformation. These observations suggests that permanent crustal and lithospheric deformation of the subducting plate occurs from the outer rise trenchward but do not allow the magnitude of weakening to be quantified.

[6] The flexural response of a plate to an applied load provides a measure of the integrated strength of the plate. The spectral characteristics of the gravity anomaly corresponding to a bathymetric load on the plate depend on the plate strength. Observations of the gravity anomaly and bathymetry can be used to calculate the admittance or transfer function. The amplitude and peak wavelength of the transfer function is indicative of plate strength and can be modeled to determine the flexural rigidity of the plate. We present the results of admittance analyses of gravity anomaly and bathymetry data from trench-parallel profiles at several distances from the trench axis in the Kermadec trench. This method provides a direct measure of the change in the flexural response of the subducting plate within the trench and a constraint on the magnitude and length scale of the reduction in plate strength.

[7] As this is an unusual application of an established technique, we first review the relevant theory for flexure and admittance analysis and present synthetic models that demonstrate the method provides robust measurements of the flexural rigidity. Next, we discuss the reasons for choosing the Kermadec trench for the first application of the method and present the swath bathymetry and free-air gravity anomaly data for four adjacent trench-parallel ship tracks within the outer trench wall and one track within the outer rise (forebulge). Finally, we present the results of admittance analyses and discuss the constraint this new method provides on the plate boundary width and reduction in plate strength within subduction zones.

2. Flexure Theory

[8] The flexural response of the plate can be studied using either forward models or inverse methods. Forward models, which assume the plate strength and predict the deflection of the plate, have been used extensively to study bending of the lithosphere perpendicular to trenches. Inverse methods, such as admittance analysis, calculate the transfer function between the observed topography and gravity, which can be compared to model predictions to determine the plate strength from the wavelength dependence of the observed deformation. In all plate-bending models the bending moment M in the lithosphere due to the slab and other forces on the plate, is equal to the integrated normal stress σ_n weighted by the depth in the plate z,

$$M = \int \sigma_n z dz, \tag{1}$$

where the normal stress depends on the constitutive relation and deformation of the plate. For a uniform elastic plate, the moment is proportional to the plate curvature,

$$M = -D\frac{d^2w}{dx^2}, \tag{2}$$

where w is the surface deflection of the plate and the proportionality constant, D, is the flexural rigidity. Similarly for a uniform viscous plate, the moment is proportional to the strain rate d^3w/dx^3, where the proportionality constant is $\eta U h^3/36$, which depends on the speed of the plate U, the viscosity η, and plate thickness h, [*DeBremaecker*, 1977; *Melosh*, 1978]. Note, that for a viscous plate the outer rise is a dynamic feature and requires motion of the plate toward the trench, while for an elastic plate the outer rise is a static feature.

[9] For bending models with nonuniform properties or stress-dependent rheology the moment will depend on the plate curvature or the strain rate and the plate strength, which may vary with position in the plate. For example, because rock has finite strength the lithosphere can deform anelastically, that is by brittle, plastic or ductile deformation, depending on the depth and the magnitude of the stress. The thickness of the plate experiencing high stresses and thus deforming anelastically increases with increasing curvature. Therefore, in regions of large curvature, the stresses will be less than that predicted by an ideal elastic plate model resulting in a lower effective flexural rigidity (lower ratio of moment to curvature).

[10] While the rheology of the lithosphere is not expected to be that of an ideal elastic plate, analysis of plate deflections using an elastic plate model allow for quantification of changes in plate strength in terms of flexural rigidity. For an ideal elastic plate the flexural rigidity is related to the elastic plate thickness

$$D = \frac{Eh^3}{12(1-\nu^2)} \tag{3}$$

by the elastic constants E and ν (see Table 1). Therefore, by analogy to the ideal elastic plate, the flexural rigidity determined by comparison of an observed trench profile to that predicted by a plate-bending model can be associated with an *effective elastic thickness*, h_e. In the trench environment, the absolute magnitude of the flexural rigidity or effective elastic thickness is not likely to be directly related to the true elastic flexural rigidity or thickness of the elastic portion of the lithosphere, but does represent a consistent measure of the integrated strength of the lithosphere that can be used to constrain changes in plate strength.

[11] Deformation of the subducting plate in convergent margins has been successfully modeled as the bending of a thin plate with uniform elastic rheology [*Hanks*, 1971; *Caldwell et al.*, 1976; *Parsons and Molnar*, 1978] or viscous rheology [*DeBremaecker*, 1977; *Melosh*, 1978]. However, in some regions steep trench profiles are better fit by a uniform elastic-perfectly plastic rheology [*McAdoo et al.*, 1978; *Turcotte et al.*, 1978; *Carey and Dubois*, 1982] or layered plate structure that accounts for temperature-dependent rheology and the inability of the brittle shallow

Table 1. Parameter Notation, Value and/or Units Used in Plate Flexure and Spectral Analysis[a]

Parameter	Symbol	Value/Unit
Plate Flexure		
Flexural rigidity		
Theoretical	D	N m
Estimate	D^*	N m
Synthetic seamount	D_s	N m
Elastic plate thickness	h	km
Effective elastic thickness	h_e	km
Young's modulus	E	70 GPa
Poission's ratio	ν	0.25
Crustal density	ρ_c	2800 kg/m^3
Mantle density	ρ_m	3300 kg/m^3
Water density	ρ_w	1000 kg/m^3
Average water depth[b]	d	6000–8000 m
Crustal thickness[c]	t	7500 m
Spectral Analysis		
Wave number vector	$\mathbf{k} = (k_x, k_y)$	rad/km
Wave number magnitude	$k = \lvert\mathbf{k}\rvert$	rad/km
Bathymetry spectra	$B(\mathbf{k})$	m
Gravity anomaly spectra	$G(\mathbf{k})$	mGal
Spectral density		
Bathymetry	$S_{bb}(\mathbf{k})$	m^2
Gravity anomaly	$S_{\Delta g\Delta g}(\mathbf{k})$	mGal^2
Cross-spectral density	$S_{h\Delta g}(\mathbf{k})$	m mGal
Admittance (theoretical, estimate)	$Z(\mathbf{k})$, $Z^*(\mathbf{k})$	mGal/m
Admittance error	$\sigma(\mathbf{k})$	mGal/m
Coherence squared (coherence)	$\gamma^2(\mathbf{k})$	0–1
Phase of admittance	$\phi(\mathbf{k})$	−90–90
Admittance misfit	ε	mGal/m

[a]Parameter values are listed where a single value is used throughout the study.
[b]A different average depth is determined for each profile.
[c]Average crustal thickness for slow spreading ridges [*White et al.*, 2001].

crust to support large tensional stresses [*Chapple and Forsyth*, 1979; *Goetze and Evans*, 1979]. While models with an elastic-perfectly plastic rheology are most successful at fitting trench profiles and are consistent with experimental rock mechanics [*Forsyth*, 1980], steep trench profiles can also be fit by a purely elastic model with a decrease in the elastic strength trenchward of the forebulge [*Judge and McNutt*, 1991]. However, as noted by *Judge and McNutt* [1991], regardless of rheology, trench-perpendicular profiles average over the physical properties of the plate at the length scale of bending, separating the plate into regions simply decreases the averaging length scale. The ability to fit a given trench profile with various plate rheologies or assumptions about lateral variation in the strength indicates that analysis of trench-perpendicular profiles is not able to constrain uniquely the length scale and magnitude of plate weakening within a subduction zone. Instead a method that allows for direct, local measurements of the plate strength is required.

[12] Flexural rigidity measurements of oceanic plates using topography-gravity admittance estimates from ship track profiles have been made in a large number of studies (see *Watts* [2001] for a summary). In regions where the topographic load primarily varies in one direction, one-dimensional (1-D) analysis of individual profiles is appropriate (e.g., perpendicular to a spreading center or chain of seamounts [*Dorman and Lewis*, 1970; *McKenzie and Bowin*, 1976; *Watts*, 1978]). If the topographic load varies in two directions, then 2-D analysis using swath bathymetry over a large area is required (e.g., a large seamount or ridge axis [*McNutt*, 1979]). This method provides direct, localized measurement of plate strength along each profile or for each region.

[13] Determining the change in flexural rigidity across a narrow zone parallel to a trench, however, presents a unique challenge for both methods described above. First, there is a large, but uniform topographic feature parallel to the plate boundary, namely the trench. Second, the region of interest has a large aspect ratio, less than ∼200 km wide perpendicular to the trench and ∼1000 km long parallel to the trench. Therefore fully 2-D spectral analysis is not appropriate, as a nonisotropic resolution would be obtained, which would be limited in the wave number domain by the shortest dimension. Finally, as discussed above, plate-bending models applied to trench-perpendicular ship tracks are also not capable of isolating changes in flexural strength along the profile [*Judge and McNutt*, 1991; *Levitt and Sandwell*, 1995].

3. Method

[14] We present a method for measuring the change in plate strength with distance from the trench axis using one-dimensional admittance analysis of a series of adjacent trench-parallel tracks. Plate strength is estimated in terms of flexural rigidity for a simple oceanic plate model including a single crustal layer overlying a denser lithosphere. This method addresses the challenges posed by the 3-D geometry of a subduction zone, while providing better estimates of plate boundary width and change in strength of the subducting plate at convergent margins.

3.1. Spectral Analysis of Bathymetry and Gravity

[15] The flexural rigidity for a portion of the seafloor can be estimated from spectral analysis of the bathymetry and free-air gravity anomaly along 1-D profiles or 2-D surveys. For a given load on the seafloor (e.g., seamount, abyssal hill bathymetry), the relationship between the observed bathymetry and free-air gravity anomaly is determined by the mode of compensation and elastic support. Mathematically, the gravity anomaly due to an uneven, nonuniform layer can be written as the sum of an infinite series of Fourier transforms,

$$G(\mathbf{k}) = 2\pi\Gamma(\rho_1 - \rho_2)e^{-\mathbf{k}d}\sum_{n=1}^{\infty}\left(\frac{|\mathbf{k}|^{n-1}}{n!}F\{t^n(\mathbf{r})\}\right), \quad (4)$$

where d is the average depth of the area, Γ is the gravitational constant, $\mathbf{k}$ is the wave number vector $\{k_x = 2\pi/\lambda_x, k_y = 2\pi/\lambda_y\}$ and $F\{t^n(\mathbf{r})\}$ is the Fourier transform of the nth power of the layer topography [*Parker*, 1972]. For a simple elastic model of the oceanic lithosphere, including a single crustal layer, the free-air gravity anomaly will depend on the amplitude of the bathymetry $b(\mathbf{r})$ and the topography on the Moho $m(\mathbf{r})$,

$$G(\mathbf{k}) = Z(\mathbf{k})B(\mathbf{k}) + N(\mathbf{k}, b) + M(\mathbf{k}, \mathbf{m}), \quad (5)$$

where $B(\mathbf{k})$ is the Fourier transform of bathymetry. In this case, the gravity anomaly depends on a linear term due to both the bathymetry and Moho topography given by the

admittance function $Z(\mathbf{k})$ and two nonlinear terms due to the bathymetry, $N(\mathbf{k}, b)$, and due to the Moho topography, $M(\mathbf{k}, m)$ [*McNutt*, 1979; *Lyons et al.*, 2000]. All three terms depend on the density contrasts across each of the layers. In addition, the admittance function depends on the flexural rigidity of the plate.

[16] Equation (5) can be used to predict the gravity anomaly from the observations of bathymetry and Moho topography. Alternatively, equation (5) can be inverted to determine the flexural rigidity of the lithosphere. *Lyons et al.* [2000] have shown that for prediction of the gravity anomaly, the contribution from the nonlinear Moho topography term is small (<2%) and can be ignored, but the nonlinear term due to bathymetry given by

$$N(\mathbf{k}, b) = 2\pi\Gamma(\rho_c - \rho_w)e^{-\mathbf{k}d}\sum_{n=2}^{\infty}\left(\frac{|\mathbf{k}|^{n-1}}{n!}F\{b^n(\mathbf{r})\}\right) \quad (6)$$

can be significant where the height of bathymetry is close to the mean depth (e.g., 20–30 mGal over a seamount of height of 3.6 km) [see also *Parker*, 1972]. Including the nonlinear bathymetry term when inverting for the flexural rigidity, however, does not improve the estimate of flexural rigidity [*Lyons et al.*, 2000]. Therefore, for the purposes of estimating the flexural rigidity, the gravity anomaly is linearly related to the bathymetry by the admittance function,

$$G(\mathbf{k}) = Z(\mathbf{k})B(\mathbf{k}), \quad (7)$$

while for the purposes of predicting the gravity anomaly from the bathymetry, the nonlinear bathymetry term should be included,

$$G(\mathbf{k}) = Z(\mathbf{k})B(\mathbf{k}) + N(\mathbf{k}, b). \quad (8)$$

Equation (8) expressed as a function of the wave number vector is applicable to 2-D surveys of a region. The same analysis can be applied to 1-D profiles, under the assumption that bathymetric features extend infinitely in the direction perpendicular to the profile. In practice, using a 1-D approximation over large 2-D features such as seamounts will lead to an underestimate of the predicted gravity anomaly or an overestimate of the flexural rigidity of the plate [*Lyons et al.*, 2000]. Therefore all 1-D estimates of the flexural rigidity in this study are strictly upper bounds.

3.2. Admittance Analysis

[17] The admittance function, also referred to as the transfer function, is a wavelength-dependent function that depends on the mode of compensation and elastic response of the lithosphere. As an example, for Airy isostatic compensation (no elastic support), the admittance function is [*Watts*, 2001]

$$Z(k) = 2\pi\Gamma(\rho_c - \rho_w)e^{-kd}\left(1 - e^{-kt}\right). \quad (9)$$

The admittance approaches zero at long wavelengths due to isostasy and at short wavelengths due to attenuation of the gravity anomaly with depth. The first exponential term is for the attenuation due to the water depth d. The second exponental term is for the attenuation from the compensating interface at the base of the crust with a crustal thickness t.

[18] The admittance function for an elastic plate composed of a buoyant crustal layer and a denser lithospheric layer is a modification of the Airy isostatic response, which is local, to the flexural response, which is regional,

$$Z(k) = 2\pi\Gamma[\rho_c - \rho_w]e^{-kd}\left(1 - \Phi(k)e^{-kt}\right), \quad (10)$$

where

$$\Phi(k) = \left[\frac{Dk^4}{(\rho_m - \rho_c)g} + 1\right]^{-1} \quad (11)$$

is the isostatic flexural response function. The flexural admittance reduces to the Airy isostasy response as the flexural rigidity approaches zero. The peak wavelength and amplitude of the flexural admittance is controlled by the flexural rigidity. Flexural rigidity is related to the effective elastic thickness

$$D = \frac{Eh_e^3}{12(1 - \nu^2)} \quad (12)$$

by the elastic parameters for the plate (Table 1). Note, this equation is the same as equation (3) except h_e is substituted for h.

[19] This model of isostatic flexural compensation is a single-layer model in which we are assuming that the crust-mantle boundary is the compensating interface, that there are no internal loads, and that the topography and gravity anomaly at a given wavelength are linearly proportional. Other possible models could include multiple compensating interfaces, internal loads and higher-order (nonlinear) terms in the admittance [*Forsyth*, 1985; *McNutt*, 1979]. This choice of a simple layered structure is appropriate for oceanic lithosphere, which is not expected to have internal or subsurface loads unless underplating due to volcanism has occurred. Choice of a more complex model could lead to different values for the absolute magnitude of the inferred flexural rigidity. However, as stated earlier, we are using the flexural rigidity as a proxy for the strength of the plate and are concerned mainly with the change in the strength of the plate. The simple elastic plate model is sufficient for this purpose.

[20] Spectral analyses of observed bathymetry and gravity anomaly to predict the admittance function have been used in many settings including 1-D and 2-D analyses in the oceans [*McKenzie and Bowin*, 1976; *Watts*, 1978; *McNutt*, 1979] and continents [*Forsyth*, 1985; *McKenzie and Fairhead*, 1997]. Recent modifications using multitaper estimates of the cross-spectral density have made possible the analysis of shorter profiles through a more complete and homogeneous extraction of information from the entire profile or survey region [*Simons et al.*, 2000]. Following *Simons et al.* [2000], the admittance is calculated as,

$$Z^*(k) = \frac{S_{b\Delta g}(\mathbf{k})}{S_{bb}(\mathbf{k})}, \quad (13)$$

where the superscript asterisk denotes estimates made from observations. The spectral density functions, $S_{b\Delta g}$ and S_{bb}, are estimated with the multitaper method using Slepian windows [see *Simons et al.*, 2000, and references therein]. We use four Slepian windows with a space-bandwidth product, $NW = 2$, and no weighting of the tapered estimates. There are N samples per profile, determined by the length of the profile and the sampling interval Δx (2 km).

[21] Three additional spectral parameters are used to quantify the quality of the admittance estimates: the coherence squared (hereafter the coherence),

$$\gamma^2(\mathbf{k}) = \frac{\left|S_{b\Delta g}(\mathbf{k})\right|^2}{S_{\Delta g\Delta g}(\mathbf{k})S_{bb}(\mathbf{k})}, \tag{14}$$

the phase of the admittance,

$$\phi(\mathbf{k}) = \tan^{-1}\left(\frac{Re(Z^*(\mathbf{k}))}{Im(Z^*(\mathbf{k}))}\right), \tag{15}$$

and the formal error for the admittance estimates [see *Simons et al.*, 2003, and references therein]

$$\sigma(\mathbf{k}) = \sqrt{\frac{|Z^*(\mathbf{k})|^2(1-\gamma^2(\mathbf{k}))}{2k\gamma^2(\mathbf{k})}}. \tag{16}$$

The theoretical coherence is identically one for single-layer elastic plate models, as used in this study. Coherence values less than one indicate departure from this noise-free, linear and single-layered model. At short wavelengths the coherence is expected to approach zero due to significant attenuation of the gravity anomaly and decreased signal-to-noise ratio. At long wavelengths the response differs from the simple model assumptions as the gravitational response to the seafloor topography competes with the effects of isostasy. For the linear model, the phase is expected to be zero. Low coherence (less than 0.5) or high coherence along with large phase (greater than 30°) indicates that the noise in the data is too large or the length of a profile is insufficient to provide a robust estimate of the admittance.

4. Assessment of Plate Strength: Determination From Trench-Parallel Profiles

[22] There are three important issues that arise when assessing the ability of admittance estimates from 1-D trench-parallel ship tracks to determine accurately the present-day flexural rigidity along a single track. First, the track length needs to be sufficient to accurately measure the rigidity using the spectral analysis. Second, given the steep trench-perpendicular topography and gravity anomaly deviations in the ship track from a trench-parallel path can introduce an erroneous signal into the observations of similar magnitude and wavelength as the real bathymetry and gravity anomaly. Third, a challenge arises in determining whether or not the flexural rigidity estimate reflects the present-day strength of the plate or records the strength of the plate at the time of an earlier loading event. We will describe this third challenge in more detail below, before explaining how each of these issues can be tested using synthetic models.

[23] The flexural compensation model described above assumes that the topographic load and associated deformation of the plate reach equilibrium soon after loading takes place, at which time the deformation and gravitational response are "frozen in." Therefore the admittance analysis can only measure the flexural rigidity at the time of loading. For example, analysis of a seamount that is 40 million years old that sits on lithosphere that is 100 million years old would give the flexural rigidity of the lithosphere when it was 60 Myr old, the age at the time of loading. In general, the present-day flexural rigidity of the plate is expected to be larger than this value, as the plate cools, thickens and stiffens with age. However, if subsequent loading of the plate occurs that is sufficiently large as to weaken the plate, then the flexural deformation due to the old topographic load could change as the load reequilibrates with the weaker plate. In this case measurement of the flexural rigidity would give the value at the time of the second deformation event.

[24] Within the trench, the large plate bending stresses due to subduction will dominate the flexural response of the lithosphere. However, the smaller-scale seafloor topography constitutes another load on the plate and is a combination of relict topography formed before the seafloor entered the subduction zone (abyssal hills and seamounts) and actively forming topography due to faulting. In other words, there is mixed loading. The gravitational signal (and admittance) will depend on the response of both types of topography to any change in plate strength. One possibility (case 1) is that the weakening is not sufficient for reequilibration of the relict topography. In this case the admittance analysis compares the gravitational signal to a topographic signal that includes loading events that occurred at an earlier time when the plate is expected to have had a lower plate strength and newly formed topography with a higher expected plate strength. A second possibility (case 2) is that the plate-bending stresses are large enough to weaken the plate and the relict topography reequilibrates with the present-day strength of the plate. In this case, the admittance analysis will constrain the present-day flexural rigidity of the plate. To address this third challenge, synthetic tests are used to evaluate our ability to distinguish between the two mixed loading cases and therefore to determine if we can accurately measure the present-day flexural strength of the plate.

[25] For the Kermadec trench we need to assess the contribution of relict topography including abyssal hill topography and seamounts. First, abyssal hill topography, which is perpendicular to the trench, formed at the ridge and has a low expected flexural rigidity associated with the young age of the plate at the time this deformation is frozen in (5–10 Myr after forming at the ridge axis). However, this does not affect the admittance estimates since these wavelengths (10–15 km) are much smaller than the peak response of the admittance curve for reasonable values of the flexural rigidity ($D > 10^{19}$ N m). Second, a moderately sized seamount with a known age of 55 Ma [*Ballance et al.*, 1999] is traversed by three of the five ship track profiles. The age of the subducting plate is 80–100 Ma [*Billen and Stock*, 2000]; therefore the age of the plate at the time the seamount formed is ~45 Ma. The expected flexural rigidity of a plate with an age of 45 Ma is $D \approx 10^{22}$ N m, whereas a

value of $D \approx 10^{24}$ N m is expected for the present-day age of the subducting plate [*Caldwell and Turcotte*, 1979]. Therefore, if significant weakening of the plate has not occurred, we would expect the admittance analysis to return a value of $D \approx 10^{22}$ N m. However, if significant weakening of the plate has occurred, then we would expect the admittance analysis to return a value of $D < 10^{22}$ N m. Synthetic tests are used to demonstrate that these two cases can be distinguished.

5. Tests With Synthetic Data

[26] Three types of synthetic tests were developed to quantify the influence that each of the issues described above has on the admittance and flexural rigidity estimates. Test 1 assesses the limitations on estimating flexural rigidity for a given track length. Test 2 determines how deviations in the ship track from a trench-parallel path influence the estimate of the rigidity and how to recognize this effect in the admittance curves. Test 3 determines under what circumstances the present-day flexural strength can be determined and how to recognize mixed loading in the admittance curves. Determination of the predicted flexural rigidity from the admittance curves is quantified by calculating the misfit,

$$\epsilon = \frac{\sum_k^N (Z^*(k) - Z(k))^2}{N \sum_k^N Z(k)}, \tag{17}$$

between the predicted admittance Z^* and the theoretical admittance Z for a range of flexural rigidities as appropriate for each test.

5.1. Synthetic Bathymetry and Gravity Anomaly

[27] Two-dimensional synthetic bathymetry and free-air gravity anomaly (hereafter gravity anomaly) are designed to include the main features encountered along the Kermadec trench including (1) the trench, (2) the incoming abyssal hills oriented perpendicular to the trench, (3) topography due to trench-parallel active faulting, and (4) several small to moderate sized seamounts along the trench wall. A short summary of the synthetic bathymetry and gravity anomaly specifications are given below. The details are given in Appendix A.

[28] Each contribution to the synthetic bathymetry is specified independently and then summed. The trench topography is calculated from the analytic expression for a thin elastic plate constrained to match the overall shape of the Kermadec trench. The abyssal hill topography (perpendicular to the trench) and active faulting topography (parallel to the trench) are each defined as products of sinusoids with wavelengths chosen to match the observed fault spacing and power spectra of the topography (see Figure 5a in section 6). The seamounts are modeled as 2-D Gaussian loads on an elastic plate with specified flexural rigidity D_s. The synthetic seamount topography is given by the sum of the Gaussian seamount topography and the plate deflection.

[29] The synthetic gravity anomaly is calculated from the synthetic bathymetry. The contribution from the trench profile is calculated using a modified Bouguer approximation. The other contributions are calculated using the 2-D flexural response function for a simple elastic plate (equation (10)). Finally, although the active faulting topography is included in all the synthetic tests, because this topography is parallel to the trench it can only influence the results for the tests with tracks that deviate from a trench-parallel path. In this case, however, the small change in the apparent wavelength of these features is not sufficient to cause a noticeable change in the admittance curves.

[30] The 2-D synthetic gravity anomaly is given in Figure 1a. Figures 1b and 1c show profiles through the synthetic bathymetry and gravity anomaly that are parallel (A-A′) and perpendicular (B-B′) to the trench and along a synthetic ship track (synthetic ship track) that deviates from a trench-parallel path. For each of the synthetic tests the full 2-D synthetic gravity anomaly and bathymetry is calculated for a given flexural rigidity. The spectral analysis of the 1-D trench-parallel or ship track profile is performed to determine how well the analysis of 1-D profiles predicts the input flexural rigidity used to make the 2-D synthetic data.

5.2. Ship Track Length

[31] Flexural compensation occurs regionally at wavelengths determined by the flexural rigidity of the plate. The peak response is at intermediate (150–500 km) wavelengths. The amplitude of the response decreases at short (<50 km) wavelengths due to attenuation and decreases at long wavelengths (>500 km) due to isostasy. Long tracks are necessary to measure the response of the lithosphere at wavelengths beyond the peak response so that the full shape of the admittance curve can be determined. However, the length of a ship track parallel to the trench is limited by the length and geometry of the trench.

[32] Test 1 compares 1-D estimates of the flexural rigidity D^* for trench-parallel ship tracks through the synthetic data to the input value of the flexural rigidity D (Table 2 and profile A-A′ in Figure 1). For a track length of 1000 km and an input flexural rigidity $D > 10^{22}$ N m, the 1-D estimate of the flexural rigidity underestimates the input value by a factor of 10–100 (Figure 2a). If $D < 10^{22}$ N m, then a track length of 1000 km is sufficient to measure the input flexural rigidity because the regional compensation due to flexure occurs at shorter wavelengths for lower values of D. In general, if the peak in the admittance curve (controlled by D) is at a wavelength greater than half the track length, then D^* will be smaller than D. Tracks with admittance estimates that are influenced by track length are characterized by a sharp drop in admittance values at intermediate wavelengths (Figure 2b, test 1-7). This change in the shape of the admittance curve makes it possible to recognize when the track length is insufficient to recover the true flexural rigidity.

5.3. Deviations From a Trench-Parallel Path

[33] Test 2 explores the influence of deviations of the ship track from a trench-parallel path for three examples with small (2 km) and large (10 km) deviations of the path at long (2000 km) and intermediate (250 km) wavelengths (Table 2 and synthetic ship track in Figure 1). An artificial signal is introduced into the profiles in two ways. First, deviations in the ship track increase the apparent wavelength of the trench-perpendicular abyssal fabric, shifting the peak in the predicted admittance curves to higher values.

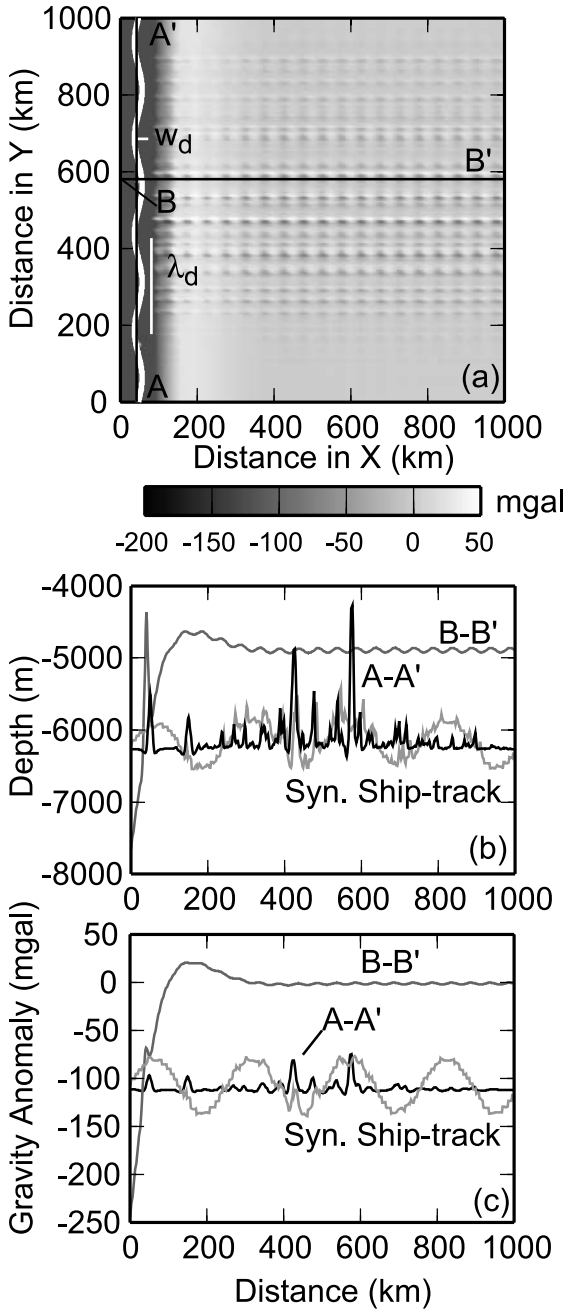

Figure 1. (a) The 2-D synthetic free-air gravity anomaly. Thick white curve denotes location of synthetic ship track with deviation from a trench-parallel path at wavelength λ_D and amplitude w_d. (b) Profiles through synthetic bathymetry for trench-parallel profile A-A′ (black), trench-perpendicular profile B-B′ (dark gray) and the synthetic ship track (pale gray). (c) Same as Figure 1b but for synthetic free-air gravity anomaly.

However, the change in the apparent wavelength is small and at short wavelengths, so this shift does not change the admittance curve significantly. Second, apparent topography and apparent gravity anomalies are introduced at the wavelength of the ship track deviation λ_d due to the track-perpendicular slope of the topography and the gravity anomaly from the trench. Because these artificial signals are perfectly correlated at a single wavelength, a spike in the admittance estimate occurs at λ_d and contaminates nearby estimates.

[34] Both long- and intermediate-wavelength deviations of the ship track from a trench-parallel path increase the estimate of the flexural rigidity by a factor of 10–100 with respect to the input value. For example, a deviation of just 2 km from a trench-parallel profile at a wavelength of 250 km (test 2-3) causes at a spike of 0.06 mGal/m in the admittance estimate (Figure 2c). This synthetic test illustrates a case where the deviation continues for the full length of the ship track and therefore has a maximum effect. Small (w_d < 1000 m) short-wavelength deviations (λ_d < 10 km) may not cause a noticeable effect given other sources of noise in the data. Designing ship tracks that follow trench-parallel isograds in the long-wavelength topography and gravity anomaly minimizes the influence of ship track path deviations. If deviations in the profile are present but not recognized, then our estimate of the flexural rigidity is an upper bound.

5.4. Present and Past (Mixed) Loading

[35] Test 3 explores the effects of mixed loading for the two cases described above. In both tests, the flexural rigidity used to calculate the initial plate deformation due to the seamount load is $D_s = 10^{22}$ N m, the expected flexural rigidity for a plate with an age of 45 Myr. In test 3-1 (case 1) the synthetic gravity anomaly is calculated from the transfer function with a flexural rigidity $D = 10^{24}$ N m for the combined topography of the trench, abyssal hills and seamount. The admittance estimate along a 1-D trench-parallel profile is then compared to the true 2-D admittance curves. The same procedure is used to create the synthetic data for test 3-2 (case 2), which tests the admittance response for a decrease in the strength of the plate to $D = 10^{19}$ N m after the initial loading by the seamount.

[36] The 1-D admittance estimate for test 3-1 shows a mixed response characterized by a flattened peak at λ = 100–250 km, corresponding to the peaks for the admittance curves with $D = 10^{22}$–10^{24} N m. Some of this flattening may be due to the difference in the flexural response of the seamount in 2-D versus the 1-D profile. This admittance curve reflects the initial deflection of the plate by the seamount that is frozen in soon after the time of loading. Further thickening of the elastic core of the plate does not change the flexural support for this load. In this scenario, the admittance estimate will only give a lower bound on the flexural rigidity because it is not able to detect the subsequent increase in plate strength due to cooling.

[37] The 1-D admittance estimate for test 3-2 recovers the low flexural strength reflecting a reduction of plate strength within the trench with only a small deviation of the admittance curve at longer wavelengths (Figure 2d). Unlike test 3-1, in which the seamount loading response is frozen in, test 3-2 assumes that the seamount load (and incoming abyssal hill bathymetry) reequilibrates in response to the reduction in regional (elastic) support. This results in a shift of the plate deflection to shorter wavelengths with a smaller corresponding gravity anomaly.

[38] Tests 3-1 and 3-2 demonstrate that the history of loading and changes to the plate strength due to aging or deformation control whether the present-day flexural strength can be determined. An estimate of the flexural

Table 2. Tests with Synthetic Data[a]

Test	D, N m	D_s, N m	w_d, km	λ_d, km	D^*, N m
1-1	1×10^{18}	-	-	-	9.2×10^{17}
1-2	1×10^{19}	-	-	-	8.5×10^{18}
1-3	1×10^{20}	-	-	-	1.4×10^{20}
1-4	1×10^{21}	-	-	-	7.3×10^{20}
1-5	1×10^{22}	-	-	-	2.2×10^{21}
1-6	1×10^{23}	-	-	-	3.9×10^{21}
1-7	1×10^{24}	-	-	-	6.7×10^{21}
2					
2-1	1×10^{20}	-	10	2000	3.3×10^{23}
2-2	1×10^{20}	-	10	250	1.0×10^{24}
2-3	1×10^{20}	-	2	250	1.2×10^{22}
3					
3-1	1×10^{24}	1×10^{22}	-	-	6.7×10^{21}
3-2	1×10^{19}	1×10^{22}	-	-	8.5×10^{18}

[a]Predicted flexural rigidity D^* is determined by calculating the misfit between the predicted admittance and the theoretical admittance curves for a range of theoretical flexural rigidities (see equation (17)). Test 1 is ship track length, test 2 is deviation from trench-parallel, and test 3 is mixed (present and past) loading.

rigidity at the time of loading can be determined based on plate-cooling models if both the age of the plate and the age of the seamount are known, as is the case for the profiles in the Kermadec trench. In this case, it can be concluded that an admittance estimate that gives a lower flexural rigidity value reflects the reequilibration of the topographic load in response to a reduction in the flexural rigidity of the plate.

[39] The three synthetic tests demonstrate that it is possible to obtain accurate estimates of the flexural rigidity along the outer trench wall using 1-D admittance estimates. This method requires that the ship tracks are sufficiently long (1000 km) and maintain a trench-parallel path. In addition, constraints on the age of seamount loads and the subducting plate provide an independent constraint on the flexural rigidity of the incoming plate. Short ship tracks can only provide a lower bound on the flexural rigidity, whereas ship tracks that deviate from a trench-parallel path give an upper bound.

6. Application to the Kermadec Trench

[40] The Kermadec trench has several characteristics that make it well suited for admittance analysis of trench-parallel

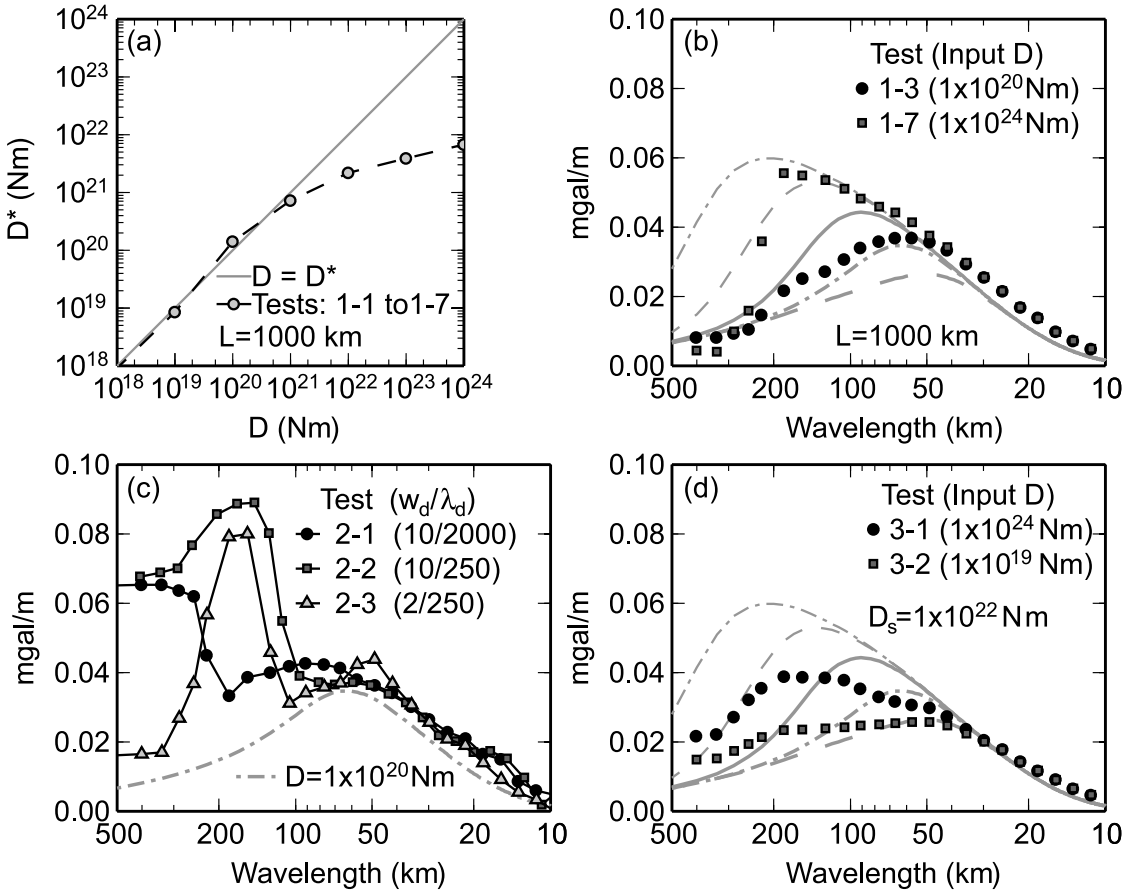

Figure 2. Admittance analyses of 1-D profiles through synthetic data given in Figure 1. Parameters used for each test are given in Table 2. (a) Test 1 predicted flexural rigidity D^* versus input flexural rigidity D for ship track length L = 1000 km. (b) Test 1 admittance estimates and theoretical admittance curves ($D = 10^{23}$ N m, thin dash-dotted; $D = 10^{22}$ N m, thin dashed; $D = 10^{21}$ N m, thick solid; $D = 10^{20}$ N m, thick dash-dotted; $D = 10^{19}$ N m, thick dashed). (c) Test 2 admittance estimates for ship tracks with a deviation from a trench-parallel path. (d) Test 3 admittance estimates for mixed loading models. Theoretical curves are the same as in Figure 2b.

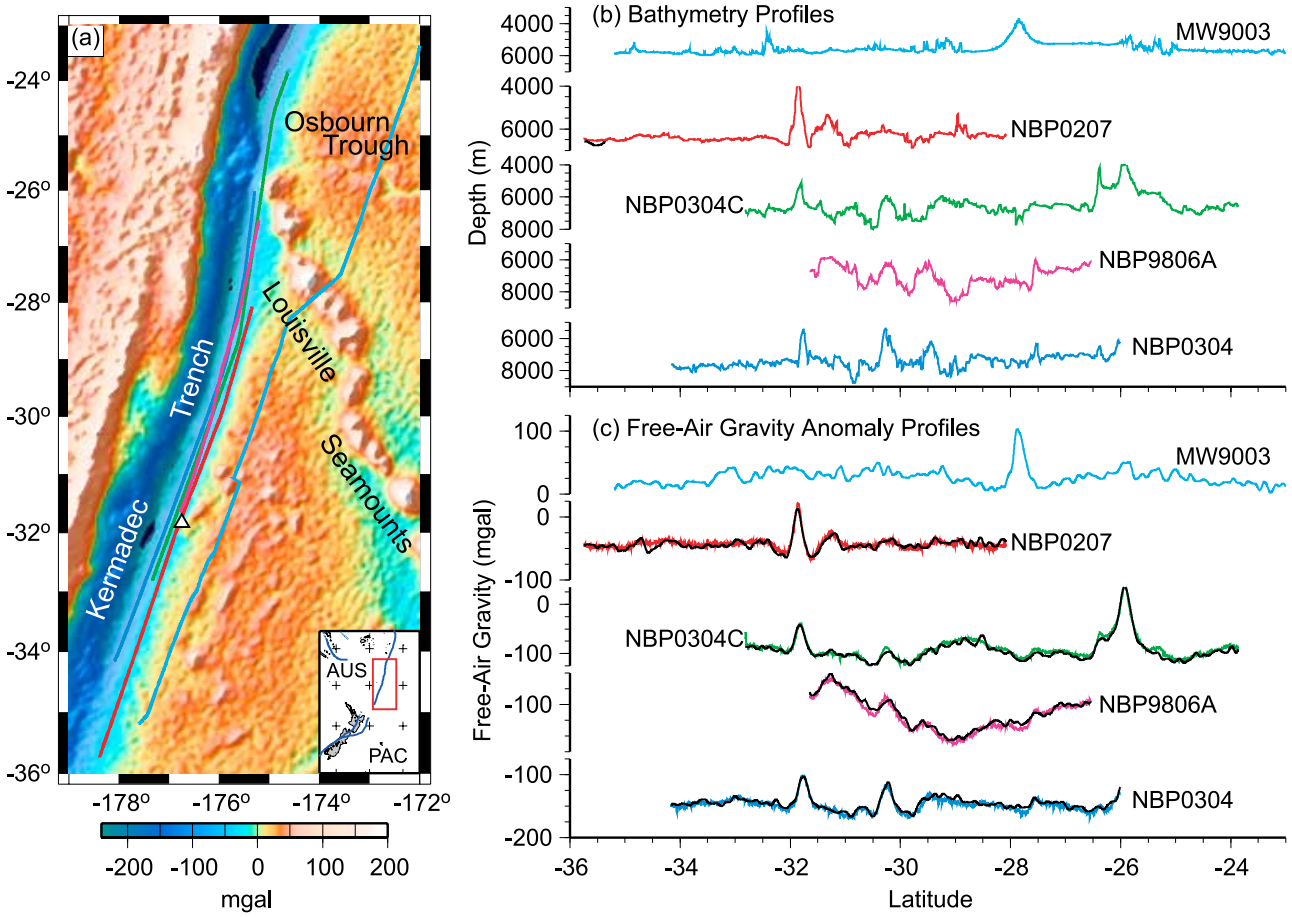

Figure 3. (a) Free-air gravity anomaly map with ship track locations: NBP0304 (blue), NBP0304C (green), NBP0207 (red), MW9003 (cyan), NBP9806A (magenta). White triangle marks location of seamount of known age at 31°50s (see text). (b) Profiles of ship track bathymetry (line color same as in Figure 3a). (c) Profiles of ship track free-air gravity anomaly (line color same as in Figure 3a) and satellite-derived free-air gravity anomaly (black profiles).

ship track data (Figure 3). The Kermadec trench is an ocean-ocean subduction zone far from a major landmass, making both the incoming plate and trench relatively sediment-poor (less than ~200 m of sediment [*Menard et al.*, 1983]). The Kermadec trench is also long (~1000 km) and relatively straight with generally homogeneous subducting seafloor (few seamounts) between the Louisville seamount (26°S) at the northern end and the northern edge of the Hikurangi plateau (37°S) at the southern end of the trench. The simple geometry makes it easier to plan and carry out surveys, and the uniformity of the seafloor eliminates complexities that could affect the admittance estimates.

[41] The loading history and characteristics of the subducting plate bathymetry entering the trench are known from previous studies in the region. The subducting seafloor formed at the now extinct Osbourn Trough with abyssal hill bathymetry oriented perpendicular to the strike of the trench and ranges in age from between 72 and 80 Ma at 25°S to greater than 100 Ma at the edge of the Hikurangi plateau at 37°S [*Luyendyk*, 1995; *Billen and Stock*, 2000; *Massell*, 2003]. The known age of the subducting seafloor provides a constraint on the maximum flexural rigidity expected for the subducting plate (1.2×10^{23}–1.0×10^{24} N m) based on age [*Caldwell and Turcotte*, 1979] and from comparison to similar estimates made for isolated seamounts emplaced on similar age seafloor far from plate boundaries [*Watts*, 2001, Table 6.1].

[42] Within the Kermadec trench there is a seamount at 31°50s and 176°45′W of known age, 54.8 ± 1.9 Ma [*Ballance et al.*, 1999]. This seamount provides a larger load on the plate than the faulting-related topography and therefore a larger signal for the admittance analysis. It also provides another load of known age and therefore an expected flexural rigidity that can be compared to the estimates made in this study. For the age of the seafloor at the time the seamount formed, the expected flexural rigidity is between 10^{22} and 10^{23} N m, depending on the degree of viscous relaxation that occurs after loading [*Watts*, 2001].

6.1. Swath Bathymetry and Free-Air Gravity Anomaly Data

[43] Four single-track surveys of the Kermadec trench with swath bathymetry and gravity anomaly measurements were made between 1998 and 2003 on the RV/IB *Nathaniel B. Palmer* (Figures 3 and 4). In 1998 we took advantage of

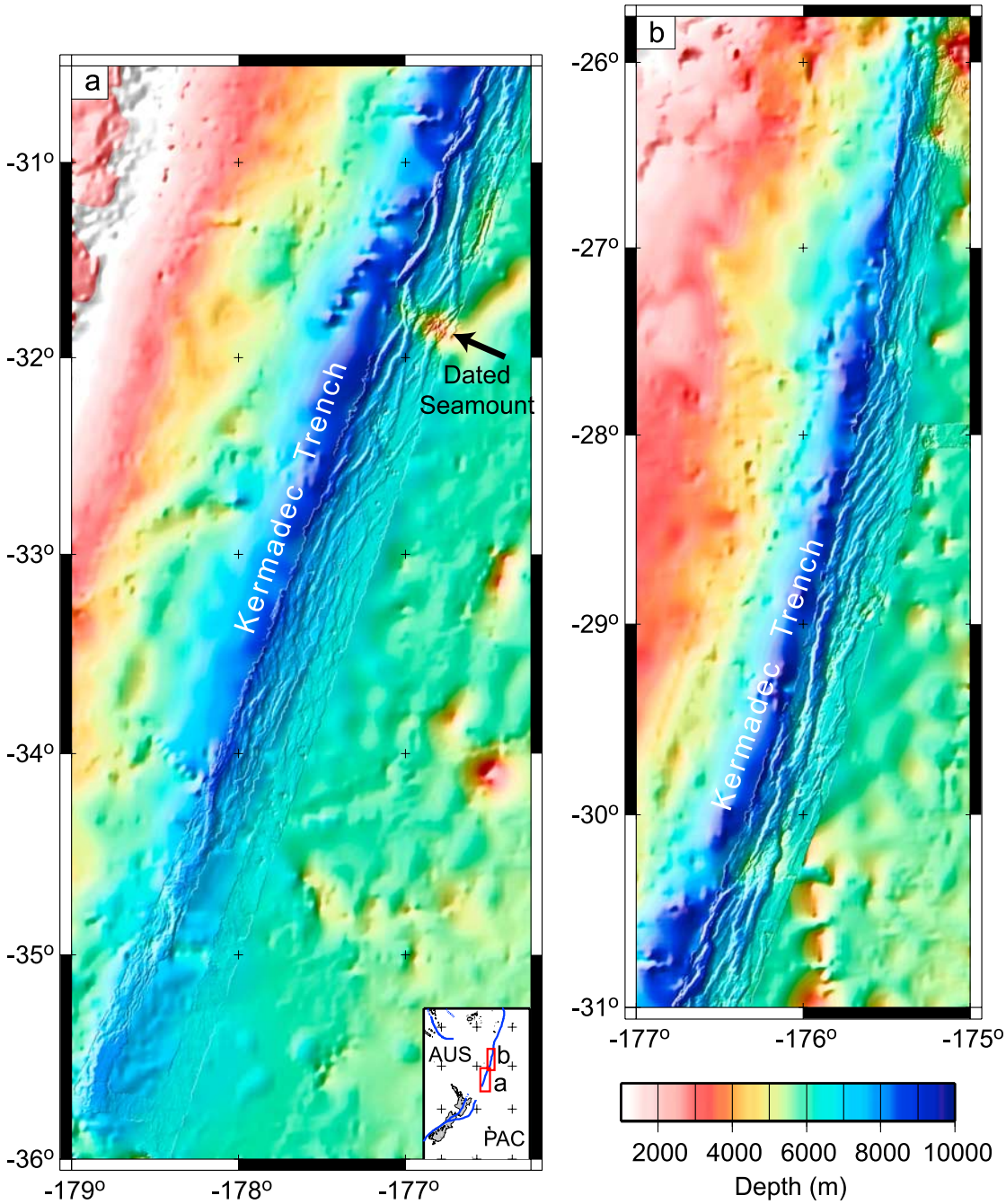

Figure 4. Swath bathymetry profiles (NBP9806A, NBP0207, NBP0304, and NBP0304C) plotted on predicted topography. Plots reveal pervasive faulting of the subducting seafloor along sinuous faults, parallel and subparallel (28–29°S) to the trench. Several faults are seen to be continuous through seamounts in the trench wall, including the dated seamount at 31°50s.

a transit to collect an initial trench-parallel ship track along the Kermadec trench (NBP9806A). This first ship track proved inappropriately oriented (deviations from a trench-parallel path) and of insufficient length (only 800 km) for admittance analysis. Based on this experience and the results of the synthetic tests, three subsequent surveys (NBP0207, NBP0304, NBP0304C) were designed for the purpose of measuring the flexural rigidity of the subducting plate at various distances from the plate boundary. Each ship track was designed to eliminate the long-wavelength contribution to the bathymetry and gravity anomaly due to the trench by following long-wavelength isograds of gravity anomaly parallel to the trench (Figures 3a and 3b). Free-air gravity anomaly data derived from satellite altimetry measurements [*Sandwell and Smith*, 1997] provided the reconnaissance data set essential for designing these surveys. While the ship board free-air gravity anomaly data include higher-resolution measurements (Lacoste-Romberg Gravi-

meter) than those derived from satellite altimetry, at similar wavelengths the two data sets are in good agreement (Figure 3c).

[44] The swath bathymetry data (Seabeam 2000 and Simrad EM120) provide the high-resolution data needed for the admittance analysis and the 2-D context for interpreting the results (Figure 4). The background bathymetry in Figure 4 is predicted topography derived from the observed satellite altimetry data and constrained by observed ship track data (version 8.2, *Sandwell and Smith* [1997]). The seafloor morphology revealed by the swath mapping demonstrates that the seafloor is undergoing active deformation with the development of long trench-parallel faults and shorter horst-graben systems. In some regions (28–29°S) the horst-graben systems form at an angle to the trench and are short wavelength (<5 km), whereas in most areas the faults are parallel to the trench and form structures roughly 5–15 km across, roughly 1–2 times the crustal thickness. The relief associated with these structures ranges from 500 to 1500 m and increases with greater depth in the trench. Fault-like structures are seen to cut through seamounts (30.5 and 32°S), further evidence of active deformation of the plate.

[45] It is important to note that if the only topographic signal in the profiles was that due to abyssal hill fabric, one would expect to measure a low flexural rigidity ($\sim 10^{19}$ N m) reflecting the formation of this topographic load near the young spreading center that formed the crust. The presence of the seamount of known age and the observed active faulting parallel to the trench (Figure 4) are two topographic loads on the plate that are known to have formed on significantly older seafloor with a larger expected flexural rigidity. While the ship tracks were designed to eliminate the large-scale signal from the trench, some of the active-faulting features are still oblique to the ship tracks. The active-faulting features include large-offset, long "trench-parallel" faults that are, in fact, sinuous in shape and short-wavelength horst-graben structures that are oblique to the ship track. Because of the short wavelength of the horst-graben structures (10–15 km), the small increase in apparent wavelength (5 km) caused by traversing the structures at a slight angle does not change the flexural rigidity estimates along these profiles. Crossing the long sinuous faults, however, can introduce erroneous signal in the same way as deviations from a trench-parallel path, in which case the flexural rigidity estimate is only an upper bound. The only profile for which this may be occurring is NBP0304C (see discussion below).

6.2. Flexural Rigidity From Trench-Parallel Ship Tracks

[46] The admittance analysis is applied to the trench-parallel ship tracks collected along the outer trench wall in the Kermadec trench (NBP9806A, NBP0207, NBP0304 and NBP0304C) and one preexisting trench-parallel ship track seaward of the forebulge (MW9003), collected on the *RV Moana Wave* by the University of Hawaii in 1990 [*U.S. Department of Commerce*, 1992]. Figure 3a shows the location of the ship tracks. Figures 3b and 3c show the bathymetry and gravity anomaly profiles. Ship board gravity anomaly data are not available for track MW9003, and satellite-altimetry derived free-air gravity anomaly data are used instead. Analysis using either the ship board or satellite-derived gravity anomaly profiles for the trench wall profiles gives the same admittance results.

[47] The admittance analyses for the profiles are summarized in Figures 5 and 6. For each profile the power spectra for bathymetry and gravity anomaly (Figures 5a and 5b) and the cross spectra are computed using the multitaper method. These are then used to compute the coherence between the bathymetry and the gravity anomaly, the phase of the admittance (Figures 5c–5g) and the admittance (Figures 6a–6c). The misfit between the admittance estimates and the theoretical curves with flexural rigidity ranging from 10^{18}–10^{24} N m is computed using equation (17) (Figure 6d). For the theoretical curves, the mean water depth appropriate for each profile is used, as this causes a small shift in the theoretical profiles. We use a constant crustal thickness of 7.5 km for all the profiles. This value gives the best fit to short-wavelength admittance estimates and is in agreement with the average crustal thickness of normal oceanic crust. These and other parameters used in computing the theoretical profiles are listed in Table 1.

[48] As noted above, ship track NBP9806A is not well suited for the admittance analysis. A jump in the power spectra and the admittance estimates occurs at a wavelength of 200 km (Figures 5a and 6c). As demonstrated by the synthetic models, a jump in the admittance estimate reflects a deviation of the ship track from trench-parallel. We present the analysis of this ship track for comparison with the other ship tracks and to demonstrate that the design of the other ship tracks is successful at minimizing the influence of track length and track path on the admittance estimates.

[49] Track NBP0304 is less than 10 km from the deepest portion of the trench. While this ship track is 1000 km long, the spectral power for the gravity anomaly flattens out at wavelengths of 50–60 km (Figure 5b). The spectral power for the bathymetry continues to increase at longer wavelengths. The difference in spectral response of the gravity and bathymetry indicates that flexural support is occurring only at short to intermediate wavelengths. The peak in the admittance curve corresponds to the wavelengths at which the gravity anomaly spectral power flattens out and is accompanied by phase values of less than 30° and coherence greater than 0.5 (Figure 5c). The slightly higher phase values and lower coherence values for this profile compared to others is in part due to the loss of resolution due to the depth of the profile (7400 m, −150 mGal). The analysis of this track gives the smallest estimate of flexural rigidity with a minimum misfit for $D^* = 2.8 \times 10^{19}$ N m (Figure 6a).

[50] Track NBP0304C lies midway up the outer trench wall (6600 m, −100 mGal), centered approximately 25 km from the trench axis. This ship track is also 1000 km long and crosses over part of the Louisville Seamount (26°S). Both the coherence and admittance analyses show evidence for mixing of responses from a low flexural rigidity region (Figures 5d and 6a: coherence and admittance peak at $\lambda = 70$–80 km) and a higher flexural rigidity region (coherence and admittance peak at $\lambda = 200$ km). This mixed response may be due to either thicker crust or stronger lithosphere beneath the Louisville Seamount, or it may be caused by signal introduced by crossing the

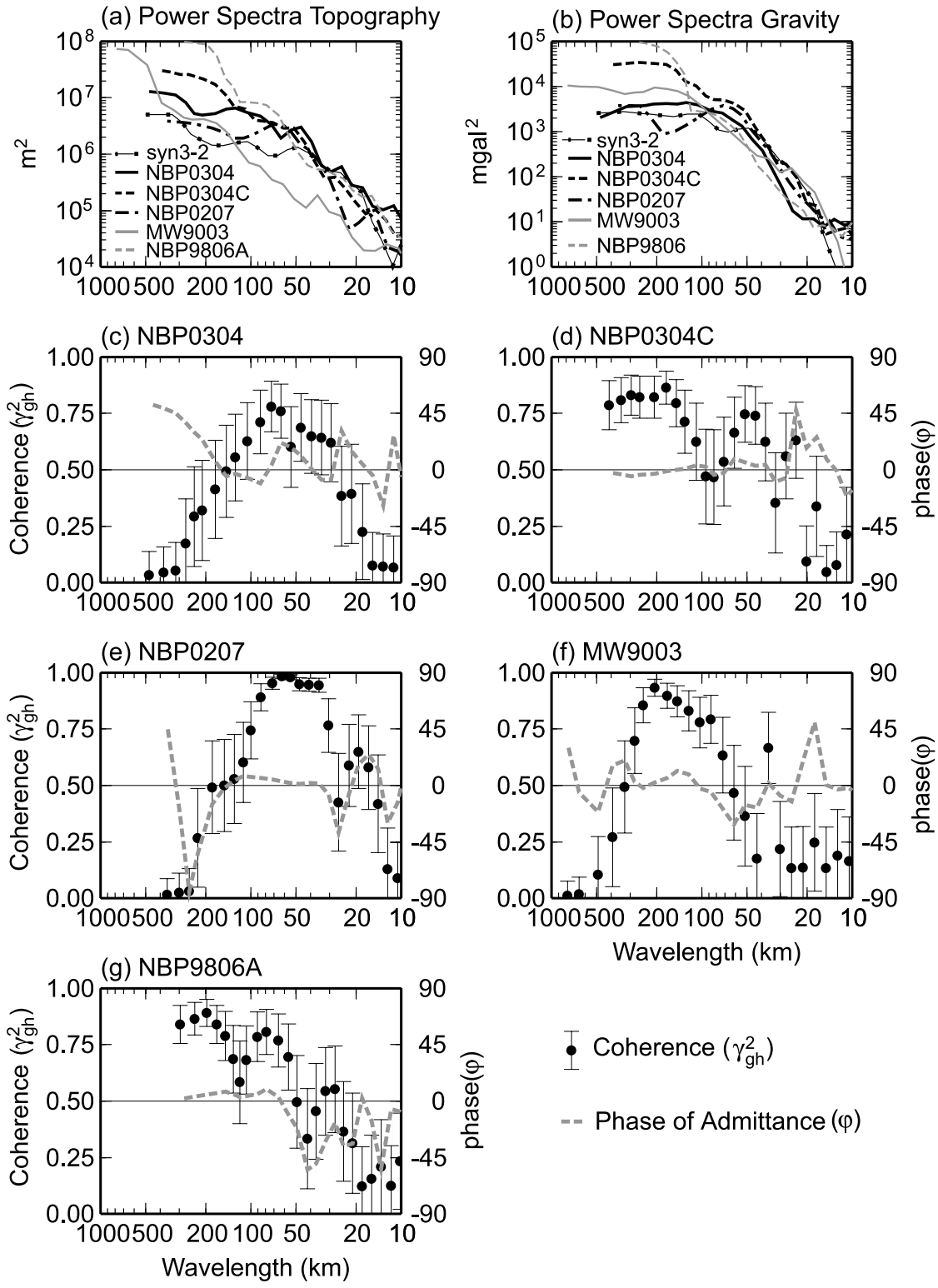

Figure 5. Summary of spectral analyses for outer trench wall and outer rise (forebulge) ship tracks: (a) Power spectra of bathymetry and (b) free-air gravity anomaly. Power spectra for synthetic data (test 3-2) are also shown. (c–g) Topography-gravity coherence (γ^2; black circles) and phase of admittance (ϕ; dashed gray) for each ship track.

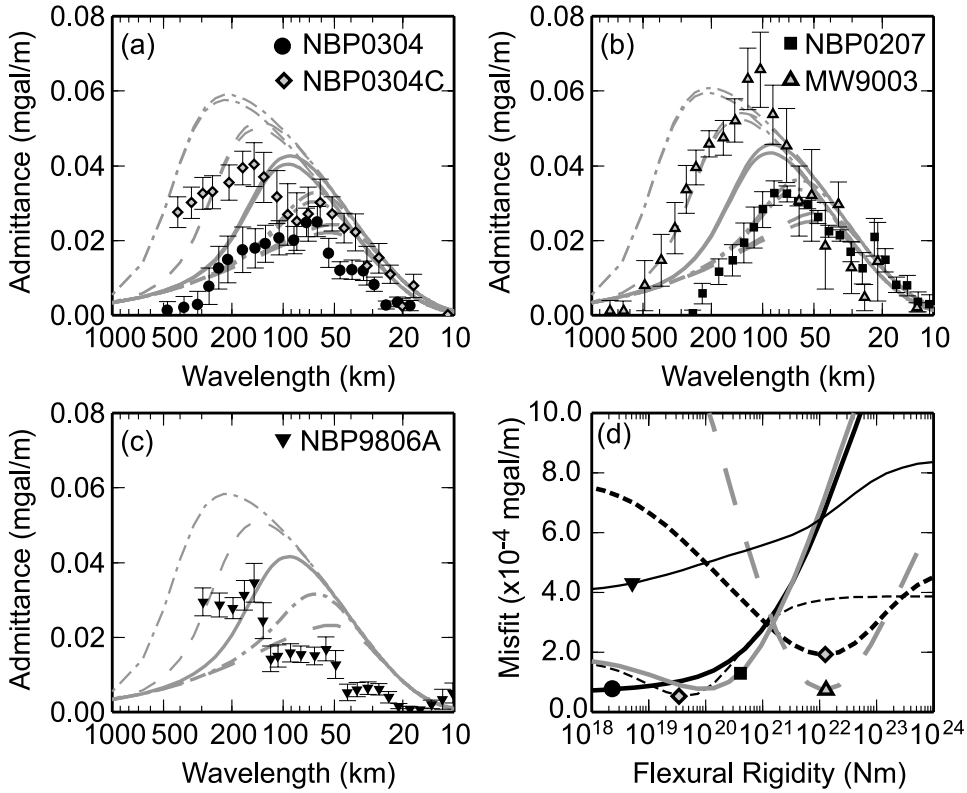

Figure 6. Admittance and flexural rigidity estimates. (a) Tracks NBP0304 (black circles) and NBP0304C (gray diamonds). Theoretical admittance curves for $D = 10^{19}-10^{23}$ N m (line types same as Figure 2). Two theoretical curves are shown for each flexural rigidity value, corresponding to the different depths of the two profiles. (b) Same as Figure 6a for tracks NBP0207 (black squares) and MW9003 (gray triangles). (c) Same as Figure 6a for track NBP9806A. (d) Admittance misfit (ε, equation (17)). Symbols marking the lines are the same as used in Figures 6a–6c: NBP0304 (black solid), NBP0304C (black dashed), NBP0207 (gray solid), MW9003 (gray dashed), NBP9806A (black thin). Two misfit curves are given for track NBP0304C: the complete admittance curve (thick black dashed) and the admittance curve at wavelengths less than 100 km (thin black dashed).

sinuous "trench-parallel" faults. The misfit curve for the entire profile gives an average flexural rigidity of 8.5×10^{21} N m (Figure 6d). However, the amplitude and location of the admittance peak at a wavelength of 70 km are best fit by $D^* = 5.0 \times 10^{19}$ N m.

[51] Track NBP0207 is approximately 50 km from the trench axis (6370 m, −50 mGal) on the shallow portion of the outer trench-wall. Compared to the two deeper profiles, the peak in the admittance estimates is shifted to a slightly higher wavelength of 90 km with a higher peak admittance (Figure 6b). Both the high coherence values (greater than 0.9 at intermediate wavelengths) and near-zero phase provide strong support that this is a robust estimate of the admittance despite the shorter length (900 km) of this profile (Figure 5e). The admittance estimates for this profile are best fit by a flexural rigidity of 7.3×10^{19} N m.

[52] The final track, MW9003, which lies outside the trench, provides an estimate of the flexural response of the crust before the plate passes through the region of largest plate curvature in the forebulge region. The admittance estimates for this profile have larger values (>0.05) with a peak near a wavelength of 150 km, which is best fit by $D^* = 1.2 \times 10^{22}$ N m (Figure 6c). The high coherence and low phase of the admittance again demonstrate that this is a robust estimate of the flexural rigidity (Figure 5f).

[53] The difference in the flexural response for ship track MW9003 compared to the three trench wall profiles is evident in the power spectra as well as the admittance estimate (Figures 5a and 5b). The power spectra of bathymetry for track MW9003 has significantly less power at short to intermediate wavelengths, while the power spectra for the gravity anomaly is similar to the three outer trench wall profiles. This is the difference expected as regional support of topography decreases within the trench, shifting the power to shorter wavelengths. As regional support wanes, isostatic support of topography is more important and leads to a decrease in the power spectra of the gravity anomaly at short to intermediate wavelengths.

[54] On the basis of the results of the synthetic tests, if there are small deviations in the ship tracks from trench-parallel paths, then the admittance estimates for the profiles within the actively deforming outer slope region provide an upper bound on the present-day flexural rigidity. However, for the ship track within the forebulge and outboard of the actively deforming trench, the admittance estimate probably provides a lower bound on the flexural rigidity corresponding

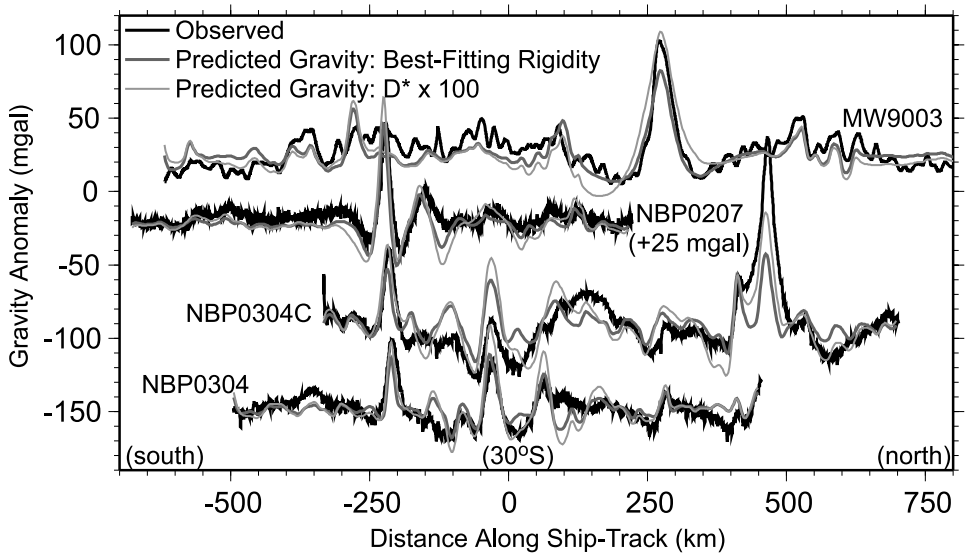

Figure 7. Comparison of observed gravity anomaly for each ship track (black) to the predicted gravity anomaly (gray) calculated from the observed bathymetry and the transfer function given by equation (10). Best fitting flexural rigidity from the admittance analysis (D^*, thick gray). Flexural rigidity of $100 \times D^*$ (thin gray). Tracks are centered at 30°S.

to the time the large seamount at 28°S (part of Louisville seamount chain) was emplaced. Since that time the lithosphere has continued to cool and the flexural rigidity should increase unless bending related stresses also affect the forebulge region.

6.3. Comparison of Observed and Predicted Gravity Anomaly

[55] The admittance analysis demonstrates that there is a large decrease in the plate strength within a short distance from the trench. The absolute values of the flexural rigidity estimates are, of course, dependent upon the choice of plate model and the dimensionality of the analysis. In particular, the very low flexural rigidity estimate within the trench, which is equivalent to an elastic plate thickness of less than 5 km may at first seem unreasonable. However, as shown in Figure 7 the gravity anomaly profiles predicted using the flexural rigidity estimates from the admittance analysis (Table 3) and equation (8) are a good fit to the observed gravity anomaly profiles. In particular the amplitude and wavelength of flexural motes for the seamounts in profile MW9003 and NBP0207 are well matched by D^*, whereas the predicted gravity anomaly for these profiles using a larger flexural rigidity ($100 \times D^*$) overpredicts the amplitude and length scale of these features. Note that the underestimate of the gravity anomaly of the seamount peaks is expected from the 1-D analysis of 2-D features [see, e.g., *Lyons et al.*, 2000].

[56] The deepest profile (NBP0304) with the lowest predicted flexural rigidity also shows good agreement in the amplitude of the small seamount at 0 km and step-like features at 50, 250 and 450 km. The mismatch that occurs at 100 km for this profile is due to steep topography parallel to the ship track that causes a graben to appear in the bathymetry profile that is not in the observed gravity profile. The admittance analysis for ship track NBP0304C indicated that there was a mixed response with two flexural rigidity values affecting the profile. Comparison of the predicted and observed gravity profiles for this ship track indicates that the lower D^* fits the southern end of the profile best, but an even lower value might provide a better match, as the amplitudes of several features are too large (from −100 to 100 km). At the northern end of the ship track a flexural rigidity value $100 \times D^*$ provides a better fit to the large seamount at 450 km. Therefore, while the low flexural rigidity values may be unexpected based on analysis of trench-perpendicular profiles using elastic plate bending profiles, this analysis demonstrates that a weak plate, with little or no elastic strength, is needed to match the observed gravity anomaly within the trench.

7. Discussion and Conclusions

[57] Previous studies of trench-perpendicular profiles of bathymetry and gravity anomaly indicated that a decrease in plate strength within subduction zones occurs due to anelastic yielding of the plate under high stress [*Turcotte et al.*, 1978; *Goetze and Evans*, 1979]. However, these studies were not able to constrain the width of the weak region or the magnitude of weakening. The admittance analyses of the four trench-parallel tracks within the Kermadec subduction zone show a decrease in the flexural rigidity from greater than 1.2×10^{22} N m to less than 2.8×10^{19} N m within less than 110 km of the trench axis. The synthetic

Table 3. Summary of Flexural Rigidity Results for the Kermadec Trench

Ship Track	Distance, km	D^*, N m	Misfit Range, N m
NBP0304	10	2.8×10^{19}	$<3 \times 10^{20}$
NBP0304C	25	3.9×10^{19}	1×10^{19} to 1×10^{20}
NBP0207	50	7.3×10^{19}	6×10^{18} to 6×10^{20}
MW9003	110	1.2×10^{22}	2×10^{19} to 4×10^{22}

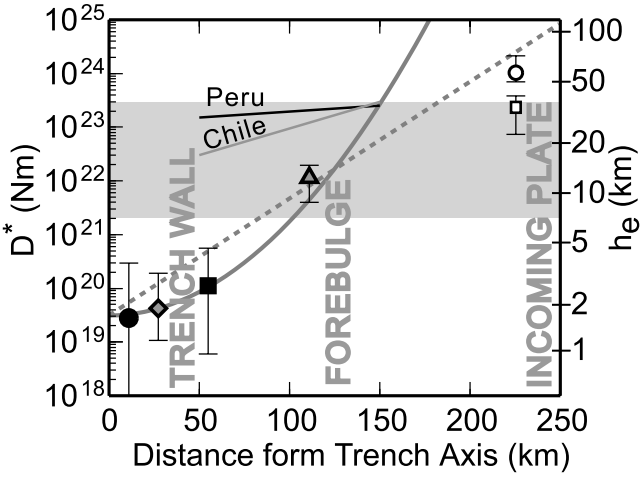

Figure 8. Summary of variation in flexural rigidity with distance from the trench axis. Solid symbols are the same as those used in Figure 6. Error bars indicate the half width at half minimum for the misfit curves given in Figure 6d. Incoming plate values are for a plate age of 100 Ma (open circle) and 40 Ma (open square) and T_e = 750°C [*Caldwell and Turcotte*, 1979]. Two lines labeled Chile and Peru connect estimates of h_e from trench-perpendicular tracks, which account for a change in h_e within the forebulge [*Judge and McNutt*, 1991]. Conversion between h_e and D* uses values from Table 1. Shaded gray region indicates range of flexural rigidity estimates for the Kermadec trench based on trench-perpendicular profiles [*Carey and Dubois*, 1982; *Levitt and Sandwell*, 1995]. Solid and dashed curves are Gaussian and exponential fits to the flexural rigidity estimates with a decay length scale of 50 and 20 km, respectively.

models demonstrate that the application of the admittance analysis to trench-parallel ship tracks provides robust estimates of the change of flexural rigidity with distance from the trench. This technique provides a new method for quantifying the width of the plate boundary zone in oceanic subduction zones where land-based measurement of strain accumulation or strain rate is not possible.

[58] Figure 8 shows the change in flexural rigidity as a function of distance from the trench. The drop in flexural rigidity by almost 3 orders of magnitude corresponds to a decrease in the effective elastic thickness by at least 15 km. The overall decay in the plate strength is best fit by either an exponential curve with a decay length scale of 20 km or a Gaussian curve with a length scale (variance) of 50 km. Future profiles within the forebulge region at a distance of 50–100 km from the trench (from existing data [*Massell*, 2003] or new surveys) are needed to determine whether the drop in flexural strength occurs gradually or sharply in this region.

[59] For comparison the results of a study of the Peru-Chile trench, which explicitly tested the influence of decreasing the effective elastic thickness trenchward of the forebulge [*Judge and McNutt*, 1991] are included in Figure 8. In Chile, the plate age is 45 Ma and the elastic plate thickness was reduced from 36.6 km to 17.0 km. In Peru, where the plate age is 30 Ma, the elastic plate thickness was reduced from 32.8 km to only 27.6 km. The flexural rigidity within the Kermadec trench measured in this study is several orders of magnitude lower than that found for the Peru-Chile trench using trench-perpendicular profiles. Although the Peru-Chile trench may have a higher flexural strength than the Kermadec trench due to a different tectonic setting, both trenches are characterized by steep trench profiles and based on the younger age of the subducting plate in the Peru-Chile trench, it is expected to have a lower flexural strength. This apparent difference is an illustration of the averaging effect of trench-perpendicular profiles, even when the profile is divided into two segments.

[60] The theory of plate tectonics describes the kinematic motion of rigid plates with relative motion concentrated at narrow zones along the plate boundaries. In convergent margins, this picture usually includes subduction of an old, strong and elastic oceanic plate along a narrow and weak plate boundary thrust fault. This picture is at odds with our results, which indicate that significant weakening of the plate occurs oceanward of the trench leaving the plate within the trench with little or no elastic strength. The large-magnitude reduction in flexural strength within the trench demonstrates that faulting of the subducting plate observed in several subduction zones is indicative of lithosphere-scale weakening of the plate rather than a purely shallow crustal response to bending of the plate. Our results suggest that significant dissipation of energy occurs within less than 100 km of the trench axis. The occurrence of large lithosphere-scale normal faulting events in the subducting plate [*Kikuchi and Kanamori*, 1995] may be one process by which this energy is dissipated and the elastic strength of the lithosphere is destroyed.

[61] Our results indicate that an appropriate rheology for the subducting plate would allow for complete loss of elastic strength within 100 km of the trench axis. The loss of elastic strength through faulting and ductile deformation under large stress requires that coupling of the slab to the plate occurs through viscous stresses and therefore the trench topography is a dynamic feature. The large reduction in plate strength that we infer for the Kermadec trench is not inconsistent with geodynamic models. Viscous models that include known sources of slab buoyancy and model plate boundaries as faults simultaneously reproduce not only the steep trench profile and the outer rise topography observed at trenches [*Zhong and Gurnis*, 1994], but also the absolute value of plate velocity [*Zhong et al.*, 1998]. Although slabs are potentially weak elastically, they still need sufficient viscous strength to drive plate motions. For example, in 2-D viscous flow models the plate speed relative to the slab descent rate drops to less than 50% for slabs that are less than 100 times more viscous than the surrounding mantle [*Billen et al.*, 2003]. Direct measurement of the reduction in plate strength as done in this study provides new evidence in support of models with complex viscous rheology that controls the mode of coupling between mantle convection and tectonic plates [*Bercovici et al.*, 2000].

Appendix A: Synthetic Bathymetry and Free-Air Gravity Anomaly

[62] The synthetic data sets are defined in a 1000 × 1000 km^2 region with the trench axis at x = 0 extending the

full length in the y direction. The synthetic bathymetry includes the trench topography $b_t(x, y)$ abyssal hill topography $b_a(x, y)$ and active faulting topography $b_{af}(x, y)$, as well as scattered seamounts of various sizes, $b_s(x, y)$. Each of these contributions to bathymetry is defined independently and the total bathymetry is given by the sum

$$b(x,y) = b_t(x,y) + b_a(x,y) + b_{af}(x,y) + b_s(x,y). \quad \text{(A1)}$$

[63] The synthetic trench bathymetry is given by the bending profile for a uniform elastic plate with a bending moment applied at one end [*Turcotte and Schubert*, 1982, equation 3-157]

$$b_t(x,y) = -\frac{\alpha^2 M_o}{2D} e^{-[(x-x_o)/\alpha]} e^{-x_o/\alpha} \frac{\sin\frac{x-x_o}{\alpha}}{\cos\frac{x_o}{\alpha}}, \quad \text{(A2)}$$

where x_o is the first zero crossing of the profile ($x = 0$), x_b is the position of the forebulge, M_o is the applied moment at $x = -x_o$ and α is the flexural parameter, which is related to the flexural rigidity by

$$\alpha = \left[\frac{4D}{(\rho_m - \rho_w)g}\right]^{1/4}. \quad \text{(A3)}$$

The applied moment can be expressed in terms of x_o, x_b, and the height of the forebulge w_b as [from *Turcotte and Schubert*, 1982, equation 3-158]

$$M_o = -\frac{2Dw_b}{\alpha^2} e^{[(x_b-x_o)/\alpha]} e^{x_o/\alpha} \frac{\cos\frac{x_o}{\alpha}}{\sin\frac{x_b-x_o}{\alpha}}. \quad \text{(A4)}$$

The parameter values controlling the bathymetry profile are chosen to match approximately the observed shape of the Kermadec trench ($x_o = 100$ km, $x_b = 160$ km, $w_b = 250$ m. See Table 1 for plate flexure parameters). It is important to note that this expression for the trench profile is only used to create a trench with the observed slope and similar shape to the observed trench with the proper amplitude for the gravity anomaly (see below). The trench bathymetry is only included to test the effect of deviations of the ship track from a trench-parallel path. The flexural rigidity used to define this profile does not enter into any of the estimates of the admittance for the synthetic data.

[64] The corresponding synthetic free-air gravity anomaly for the trench profile is given by upward continuation of a Bouguer approximation for the deflections at the seafloor and the Moho,

$$\Delta g_t(x,y) = 2\pi G(\rho_m - \rho_w) b_t(x,y)\left[B_1 e^{\frac{-d}{\alpha}} + B_2 e^{\frac{-(d+t)}{\alpha}}\right], \quad \text{(A5)}$$

where $B_1 = \left(\frac{\rho_c - \rho_w}{\rho_m - \rho_w}\right)$, $B_2 = \left(\frac{\rho_m - \rho_c}{\rho_m - \rho_w}\right)$, G is the gravitational constant and other parameters are given in Table 1 (from equation (5), *Levitt and Sandwell* [1995], and *McAdoo et al.* [1978]). This expression includes upward continuation of a constant wavelength signal from the crust-water interface at a mean depth, d, and from the crust-mantle interface at a depth, $d + t$, where t is the crustal thickness.

[65] The synthetic abyssal hill bathymetry perpendicular to the trench is taken as the product of 14 sinusoids with varying wavelengths and amplitudes,

$$b_a(y) = \prod_{i=1}^{n}\left[1 - A_i \sin\left(\frac{2\pi y}{\lambda_i}\right)\right]^2, \quad \text{(A6)}$$

where $\lambda(i)$ = [10, 20, 30, 40, 50, 60, 70, 80, 90, 100, 200, 300, 400, 500] km and $A(i) = 0.1$, for $i = 1-9$, and $A(i) = 0.2$, for $i = 10-14$. These values are chosen such that the power spectrum of the abyssal bathymetry is similar to the observed (see Figures 5a and 5b). The mean value of the bathymetry is set to zero,

$$b_a = b_a - \min(b_a), \quad \text{(A7)}$$

and the maximum amplitude of the bathymetry is set by

$$b_a = f_{ba}\frac{b_a}{\max(b_a)}, \quad \text{(A8)}$$

where f_{ba} = 400 m. The synthetic bathymetry is then tapered in the y direction,

$$b_a(x,y) = b_a \sin(\pi y/L). \quad \text{(A9)}$$

The trench-parallel variation in bathymetry, which simulates the active trench-parallel faulting topography that exists within the trench is included as a single sinusoid at the observed dominate wavelength of faulting,

$$b_{af}(x,y) = \left[1 - A(5)\sin\left(\frac{2\pi x}{\lambda_5}\right)\right]^2 \sin(\pi y/L). \quad \text{(A10)}$$

Note that this contribution to the topography can only affect synthetic ship tracks that are not exactly trench-parallel.

[66] The final contribution to the synthetic bathymetry are the seamounts modeled as 2-D Gaussian loads on an elastic plate of specified flexural rigidity D_s,

$$t_s(x,y) = \frac{e^{-\frac{1}{2}\left(\frac{(x-x_c)^2}{\sigma} + \frac{(y-y_c)^2}{\sigma}\right)}}{\sqrt{2 * \pi * \sigma}}, \quad \text{(A11)}$$

where σ defines the width of the seamount, and x_c and y_c define the location of the center of the seamount. The synthetic seamount topography is then the sum of the load topography and the deflection of the elastic plate,

$$b_s(x,y) = t_s(x,y) + w_s(x,y). \quad \text{(A12)}$$

The deflection of the plate in response to the seamount load is calculated using the 2-D transfer function for plate flexure in the spectral domain,

$$W_s(\mathbf{k}) = \left(\frac{-(\rho_c - \rho_w)g}{16D_s\pi^4\mathbf{k}^4 + (\rho_m - \rho_w)g}\right) T_s(\mathbf{k}), \quad \text{(A13)}$$

where T_s is the 2-D Fourier transform of $t_s(x, y)$. The deflection in the space domain is found by taking the 2-D inverse Fourier transform of $W_s(\mathbf{k})$. The bathymetry for

several seamounts of varying size can each be calculated in this way and then summed.

[67] The synthetic free-air gravity anomaly Δg is calculated from the synthetic bathymetry, where the total gravity anomaly is a sum of the individual contributions,

$$\Delta g(x,y) = \Delta g_t(x,y) + \Delta g_a(x,y) + \Delta g_{af}(x,y) + \Delta g_s(x,y). \tag{A14}$$

The contribution from the trench profile $\Delta g_t(x, y)$ is calculated using the modified Bouguer approximation given above, while the contributions from the abyssal hill gravity $\Delta g_a(x, y)$, active-faulting gravity $\Delta g_{af}(x, y)$ and seamount gravity $\Delta g_s(x, y)$ are calculated using the known transfer function from equation (10) for a specified flexural rigidity D.

[68] **Acknowledgments.** We are particularly grateful to Joann M. Stock for arranging the transects on the Nathaniel B. Palmer. We thank the Associate Editor, Frederick Simons, reviewer Laura Wallace, and an anonymous reviewer for their thorough reviews and insightful comments and suggestions. This work has been supported by the National Science Foundation and represents contribution 9087 of the Division of Geological and Planetary Sciences, California Institute of Technology.

References

Ballance, P. F., A. G. Ablaev, I. K. Pushchin, S. P. Pletnev, M. G. Birylina, T. Itaya, H. A. Follas, and G. W. Gibson (1999), Morphology and history of the Kermadec trench-arc-backarc basin-remnant arc system at 30 to 32°S: Geophysical profile, microfossil and K-Ar data, *Mar. Geol.*, *159*, 35–63.

Bercovici, D., Y. Ricard, and M. Richards (2000), The relation between mantle dynamics and plate tectonics: A primer, in *The History and Dynamics of Global Plate Motions*, *Geophys. Monogr. Ser.*, vol. 21, edited by M. A. Richards, R. Gordon, and R. V. der Hilst, pp. 5–46, AGU, Washington, D. C.

Billen, M. I., and J. Stock (2000), Origin and morphology of the Osbourn Trough, *J. Geophys. Res.*, *105*, 13,481–13,489.

Billen, M. I., M. Gurnis, and M. Simons (2003), Multiscale dynamic models of the Tonga-Kermadec subduction zone, *Geophys. J. Int.*, *153*, 359–388.

Caldwell, J. G., and D. L. Turcotte (1979), Dependence of the thickness of the elastic oceanic lithosphere on age, *J. Geophys. Res.*, *84*, 7572–7576.

Caldwell, J. G., W. F. Haxby, D. E. Karig, and D. L. Turcotte (1976), On the applicability of a universal elastic trench profile, *Earth Planet. Sci. Lett.*, *31*, 239–246.

Carey, E., and J. Dubois (1982), Behaviour of the oceanic lithosphere at subduction zones: Plastic yield strength from a finite-element method, *Tectonophysics*, *74*, 99–110.

Chapple, W. M., and D. W. Forsyth (1979), Earthquakes and bending of plates at trenches, *J. Geophys. Res.*, *84*, 6729–6749.

Christensen, D. H., and L. J. Ruff (1988), Seismic coupling and outer rise earthquakes, *J. Geophys. Res.*, *93*, 13,421–13,444.

Conrad, C. P., and B. H. Hager (2001), Mantle convection with strong subduction zones, *Geophys. J. Int.*, *144*, 271–288.

Conrad, C. P., and C. Lithgow-Bertelloni (2002), How mantle slabs drive plate tectonics, *Science*, *298*, 207–209.

Davies, G. F., and M. A. Richards (1992), Mantle convection, *J. Geol.*, *100*, 151–206.

DeBremaecker, J. C. (1977), Is the oceanic lithosphere elastic or viscous?, *J. Geophys. Res.*, *82*, 2001–2004.

Dorman, L. M., and B. T. R. Lewis (1970), Experimental isostasy: 1. Theory of the determination of the Earth's isostatic response to a concentrated load, *J. Geophys. Res.*, *73*, 3357–3365.

Evans, B., J. T. Fredrich, and T.-F. Wong (1990), The brittle-ductile transition in rocks: Recent experimental and theoretical progress, in *The Brittle-Ductile Transition in Rocks: The Heard Volume*, *Geophys. Monogr. Ser.*, vol. 56, edited by A. G. Duba et al., pp. 1–20, AGU, Washington, D. C.

Forsyth, D. W. (1980), Comparison of mechanical models of oceanic lithosphere, *J. Geophys. Res.*, *85*, 6364–6368.

Forsyth, D. W. (1985), Subsurface loading and estimates of the flexural rigidity of continental lithosphere, *J. Geophys. Res.*, *90*, 12,623–12,632.

Goetze, C., and B. Evans (1979), Stress and temperature in the bending lithosphere as constrained by experimental rock mechanics, *Geophys. J. R. Astron. Soc.*, *59*, 463–478.

Gurnis, M., S. Zhong, and J. Toth (2000), On the competing roles of fault reactivation and brittle failure in generating plate tectonics from mantle convection, in *The History and Dynamics of Global Plate Motions*, *Geophys. Monogr. Ser.*, vol. 121, edited by M. A. Richards, R. G. Gordon, and R. D. van der Hilst, AGU, Washington, D. C.

Hanks, T. C. (1971), The Kurile trench-Hokkaido rise system: Large shallow earthquakes and simple models of deformation, *Geophys. J. R. Astron. Soc.*, *23*, 173–189.

Jones, G. M., T. W. C. Hilde, G. F. Sharman, and D. C. Agnew (1978), Fault patterns in outer trench walls and their tectonic significance, paper presented at International Geodynamics Conference on the Western Pacific and Magma Genesis, Sci. Counc. Jpn., Tokyo.

Judge, A. V., and M. K. McNutt (1991), The relationship between plate convergence and elastic plate thickness: a study of the Peru-Chile trench, *J. Geophys. Res.*, *96*, 16,625–16,639.

Kikuchi, M., and H. Kanamori (1995), The Shikotan earthquake of October 4, 1994: Lithosphere earthquake, *Geophys. Res. Lett.*, *22*, 1025–1028.

Kobayashi, K., M. Nakanishi, K. Tamaki, and Y. Ogawa (1998), Outer slope faulting associated with the western Kuril and Japan trenches, *Geophys. J. Int.*, *134*, 356–372.

Kohlstedt, D. L., B. Evans, and S. J. Mackwell (1995), Strength of the lithosphere: Constraints imposed by laboratory experiments, *J. of Geophys. Res.*, *100*, 17,587–17,602.

Levitt, D. A., and D. T. Sandwell (1995), Lithospheric bending at subduction zones based on depth soundings and satellite altimetry, *J. Geophys. Res.*, *100*, 379–400.

Luyendyk, B. P. (1995), Hypothesis for Cretaceous rifting of East Gondwana caused by subducted slab capture, *Geology*, *23*(4), 373–376.

Lyons, S. N., D. T. Sandwell, and W. H. F. Smith (2000), Three-dimensional estimation of elastic thickness under the Louisville Ridge, *J. Geophys. Res.*, *105*, 13,239–13,252.

Massell, C. G. (2003), Large scale structural variation of trench outer slopes and rises, Ph.D. thesis, Univ. of Calif., San Diego.

Masson, D. G. (1991), Fault patterns at outer trench walls, *Mar. Geophys. Res.*, *13*, 209–225.

McAdoo, D. C., J. G. Caldwell, and D. L. Turcotte (1978), On the elastic-perfectly plastic bending of the lithosphere under generalized loading with application to the Kuril Trench, *Geophys. J. R. Astron. Soc.*, *54*, 11–26.

McKenzie, D., and C. Bowin (1976), The relationship between bathymetry and gravity in the Atlantic Ocean, *J. Geophys. Res.*, *81*, 1903–1915.

McKenzie, D., and D. Fairhead (1997), Estimates of the effective elastic thickness of the continental lithosphere from Bouguer and free-air gravity anomalies, *J. Geophys. Res.*, *102*, 27,523–27,552.

McNutt, M. (1979), Compensation of oceanic topography: An application of the response function technique to the Surveyor Area, *J. of Geophys. Res.*, *84*, 7589–7598.

Melosh, H. J. (1978), Dynamic support of the outer rise, *Geophys. Res. Lett.*, *5*, 321–324.

Menard, H. W., et al. (1983), *Initial Reports of the Deep Sea Drilling Program*, vol. 91, U.S. Govt. Print. Off., Washington, D. C.

Parker, R. L. (1972), The rapid calculation of potential anomalies, *Geophys. J. R. Astron. Soc.*, *31*, 447–455.

Parsons, B., and P. Molnar (1978), The origin of the outer topographic rise associated with trenches, *Geophys. J. R. Astron. Soc.*, *45*, 707–712.

Ranero, C., J. P. Morgan, K. McIntosh, and C. Reichert (2003), Bending-related faulting and mantle serpentinization at the Middle America trench, *Nature*, *425*, 367–373.

Sandwell, D. T., and W. H. F. Smith (1997), Marine gravity anomaly from GeoSat and ERS1 satellite altimetry, *J. Geophys. Res.*, *102*, 10,039–10,054.

Simons, F. J., M. T. Zuber, and J. Korenaga (2000), Isostatic response of the Australian lithosphere: Estimation of effective elastic thickness and anisotropy using multitaper spectral analysis, *J. of Geophys. Res.*, *105*, 19,143–19,184.

Simons, F. J., R. D. van der Hilst, and M. T. Zuber (2003), Spatio-spectral localization of isostatic coherence anisotropy in Australia and its application to seismic anisotropy: Implications for lithospheric deformation, *J. Geophys. Res.*, *108*(B5), 2250, doi:10.1029/2001JB000704.

Turcotte, D. L., and G. Schubert (1982), *Geodynamics*, 1 ed., John Wiley, Hoboken, N. J.

Turcotte, D. L., D. C. McAdoo, and J. G. Caldwell (1978), An elastic-perfectly plastic analysis of the bending of the lithosphere at a trench, *Tectonophysics*, *47*, 193–208.

U.S. Department of Commerce (1992), GEODAS Marine Geological and Geophysical Data[CD-ROM], NOAA, Natl. Geod. Data Cent., Boulder, Colo.

Watts, A. B. (1978), An analysis of isostasy in the world's oceans: 1. Hawaiian-Emperor seamount chain, *J. Geophys. Res.*, *83*, 5989–6004.
Watts, A. B. (2001), *Isostasy and Flexure of the Lithosphere*, Cambridge Univ. Press, New York.
White, R. S., T. A. Minshull, M. J. Bickle, and C. J. Robinson (2001), Melt generation at very slow-spreading oceanic ridges: Constraints from geochemical and geophysical data, *J. Petrol.*, *42*, 1171–1196.
Zhong, S., and M. Gurnis (1994), Controls on trench topography from dynamic models of subducted slabs, *J. Geophys. Res.*, *99*, 15,683–15,695.
Zhong, S., M. Gurnis, and L. Moresi (1998), Role of faults, nonlinear rheology, and viscosity structure in generating plates from instantaneous mantle flow models, *J. Geophys. Res.*, *103*, 15,255–15,268.

M. I. Billen, Department of Geology, University of California Davis, Davis, CA 95616, USA. (billen@geology.ucdavis.edu)
M. Gurnis, Seismological Laboratory, Pasadena, California Institute of Technology, CA 91125, USA. (gurnis@gps.caltech.edu)